Study on Thermal Behavior and Safety Properties of Na$_4$Fe$_3$(PO$_4$)$_2$(P$_2$O$_7$) and NaNi$_{1/3}$Fe$_{1/3}$Mn$_{1/3}$O$_2$ Cathode-Based Sodium Ion Battery

Ran Yu, Shiyang Liu, Xuehai Li, Bin Wei and Xiaochao Wu *

Department of Energy Storage, China Electric Power Research Institute, Beijing 100192, China
* Correspondence: wuxiaochao@epri.sgcc.com.cn

Abstract: Sodium-ion batteries (SIBs) share similar working principles with lithium-ion batteries while demonstrating cost advantages. However, the current understanding of their safety characteristics remains insufficient, and the thermal runaway mechanisms of different SIB systems have not been fully elucidated. This study investigated the following two mainstream sodium-ion battery systems: polyanion-type compound (PAC) and layered transition metal oxide (TMO) cathodes. Differential scanning calorimetry (DSC) was employed to evaluate the thermal stability of cathodes and anodes, examining the effects of state of charge (SOC), cycling, and overcharging on electrode thermal stability. The thermal stability of electrolytes with different compositions was also characterized and analyzed. Additionally, adiabatic thermal runaway tests were conducted using an accelerating rate calorimeter (ARC) to explore temperature–voltage evolution patterns and temperature rise rates. The study systematically investigated heat-generating reactions during various thermal runaway stages and conducted a comparative analysis of the thermal runaway characteristics between these two battery systems.

Keywords: sodium-ion batteries; thermal runaway; battery safety; layered oxide cathode; polyanion-type cathode

1. Introduction

The environmental challenges posed by prolonged fossil fuel consumption, including pollution and the depletion of non-renewable resources, have driven the development of electrical energy storage systems (EESSs) [1,2]. Consequently, grid-scale lithium-ion batteries (LIBs) have seen widespread adoption in electronic power equipment and energy storage infrastructure. This growing reliance on LIBs has significantly increased the global demand for lithium resources, resulting in a sharp rise in their market prices [3–5]. With lithium's crustal abundance at just 0.0065%—far lower than sodium's 2.74%—sodium-ion batteries (SIBs) have emerged as a compelling alternative to LIBs. Their appeal lies in sodium's cost advantages and chemical similarities in intercalation behavior to Li, enabling the adaptation of lithium-ion battery materials for sodium storage. However, the larger ionic radius of Na$^+$ (1.02 Å) compared to Li$^+$ (0.76 Å) poses significant challenges. It complicates the identification of host materials with sufficiently open frameworks to accommodate Na$^+$ and results in sluggish ionic diffusion kinetics. These limitations have made the development of high-performance, low-cost electrode materials for SIBs the central focus of current research efforts [6–8].

While electrochemical performance is essential, battery safety remains a paramount concern in real-world applications. Growing reports of fires in energy storage systems

and electric vehicles have intensified the scrutiny of battery safety protocols. For LIBs, thermal runaway mechanisms are well-documented in mature systems such as lithium iron phosphate (LFP) and ternary batteries, involving cascading exothermic reactions like solid electrolyte interphase (SEI) film decomposition, anode–electrolyte interactions, cathode breakdown, electrolyte degradation, and anode–binder reactions [9,10]. Critical factors such as cathode potential shifts during cycling [11,12], SEI film integrity and electrolyte composition [13–15], and overcharge/overdischarge conditions [16] have been shown to directly impact thermal stability and runaway progression. In contrast, SIB thermal runaway mechanisms remain poorly understood, with incomplete data on characteristic trigger temperatures and reaction pathways. Heat generation has been reported as a primary trigger of thermal runaway in SIBs. Ren et al. [17] developed a thermodynamic model using differential scanning calorimetry (DSC) to analyze heat release dynamics, while Robinson et al. [18] compared sodium-ion and lithium-ion pouch cells via accelerated rate calorimetry (ARC), revealing SIBs' significantly lower self-heating rates compared to LIBs. Collectively, these studies highlight that SIB thermal stability and heat generation vary substantially depending on anode/cathode material combinations, with electrode chemistry playing a critical role in thermal runaway [19,20].

Common cathode materials for SIBs fall into the following three categories: layered transition metal oxides (TMOs), prussian blue analogs (PBAs), and polyanion-type compounds (PACs) [21]. TMOs leverage their layered structure to enable a high sodium-ion storage capacity, but O3-phase oxides suffer from poor air stability, limiting their practical deployment. PBAs, featuring an open 3D framework, deliver a high voltage and reversible capacity. Yet their synthesis involves toxic cyanide precursors, and inherent crystalline water compromises their structural integrity. PACs exhibit an exceptional cycling stability and thermal resilience due to their rigid polyhedral frameworks, positioning them as prime candidates for large-scale energy storage systems [22–25].

In this study, we focus on TMOs and PACs—two material classes with mature synthesis protocols and a growing commercial viability in SIBs. We systematically investigate the thermal runaway mechanisms induced under different states of charge (SOCs), cycling conditions, and overcharge states, while characterizing electrolyte thermal stability. Adiabatic thermal runaway tests reveal temperature–voltage evolution patterns and identify the dominant exothermic reactions at different stages. The findings provide valuable insights for improving the safety and performance of sodium-ion batteries.

2. Experimental Section

2.1. Chemical Agents

The electrodes used in this experiment were produced by Huzhou Horizontal Na Energy Technology Co., Ltd., which included polyanionic cathode [with a mass ratio of 94:1:1:4 for $Na_4Fe_3(PO_4)_2(P_2O_7)$ (NFPP), conductive carbon black Super P (SP), carbon nanotubes (CNT), and polyvinylidene fluoride (PVDF)], layered oxide cathode [with a mass ratio of 96.5:1:1:1.5 for $NaNi_{1/3}Fe_{1/3}Mn_{1/3}O_2$ (NFM), SP, CNT, and PVDF], and hard carbon anode [with a mass ratio of 95.5:1:0.7:1:1.8 for hard carbon (HC), SP, carboxymethyl cellulose sodium (CMC), polyacrylonitrile (PAN), and styrene-butadiene rubber (SBR)]. The characterization parameters of the cathode and anode electrodes are listed in Table 1.

The pouch-type PAC SIB (based on NFPP cathode/HC anode) and LMO SIB (based on NFM cathode/HC anode) were manufactured by Huzhou Horizontal Na Energy Technology Co., Ltd. (Huzhou, China). The electrolytes used in these batteries were independently developed by this company. All batteries exhibited a capacity of 3 Ah.

Table 1. Characterization parameters of cathode and anode electrodes.

Electrodes	NFPP Cathode	NFM Cathode	Hard Carbon Anode
Areal mass density ($g\,m^{-2}$)	250	290	115
Tap density ($g\,cm^{-3}$)	1.2	3.0	0.95
Substrate	Carbon-coated Al foil	Carbon-coated Al foil	Cu gloss foil

2.2. Material Characterization and Safety Test

Differential scanning calorimetry (DSC) was employed to evaluate the thermal stability of the cathodes, anodes, and electrolytes. Taking the NFPP cathode as an example, CR-2032 coin cells were assembled with the NFPP cathode and sodium metal as a counter electrode to investigate the impact of state of charge (SOC) on the cathode's thermal stability. These cells underwent three constant-current charge/discharge cycles at 0.1 C (1 C = 90 mA g^{-1}) within a voltage range of 2.0–3.8 V using a multi-channel battery testing system (Neware BTS-2300, Hong Kong, China). Subsequently, the cells were charged to 20% SOC, 60% SOC, and 100% SOC at 0.1 C. When the electrochemcial tests were finished, the cells were disassembled in an argon-filled glovebox and the electrode materials were rinsed with dimethyl carbonate (DMC), thoroughly dried, and scraped off for the DSC measurements. The DSC measurements were conducted under a nitrogen atmosphere with a temperature ramp from 50 °C to 450 °C at a heating rate of 10 °C min^{-1}. To study the effect of cycling on thermal stability, cells cycled 50 times at 1.0 C were charged to 100% SOC and subjected to the same disassembly, cleaning, drying, and DSC procedures. For the study of the effect of overcharge abuse, cells were charged to 120% SOC at 0.1 C and processed identically. Additionally, DSC tests were performed on the 100% SOC cathode at varying heating rates (3 °C min^{-1}, 5 °C min^{-1}, and 10 °C min^{-1}), and the reaction activation energy E was calculated using the Kissinger equation.

$$\ln(a/T_p{}^2) = \ln(AR/E) - E/RT_p, \tag{1}$$

In the equation above, a denotes the heating rate; T_p represents the exothermic peak temperature; R is the universal gas constant (8.314 J·mol^{-1}·K^{-1}); A stands for the pre-exponential factor; and E corresponds to the activation energy.

The test method to assess the thermal stability of the NFM cathode was basically the same as that of the NFPP cathode. The NFM cathode and sodium metal sheet were assembled into a coin cell and subjected to three constant-current charge/discharge cycles at 0.1 C (1 C = 140 mA g^{-1}) within a voltage range of 2.5–4.1 V. Subsequently, thermal stability tests were conducted at different SOCs, after cycling, and after overcharging. It should be noted that due to the difference in the decomposition exothermic temperatures of the two cathode materials, heating rates of 10 °C min^{-1}, 15 °C min^{-1}, and 20 °C min^{-1} were used to calculate the activation energy of the NFM cathode.

The thermal stability test of the HC anode involved assembling the HC anode and sodium metal into a coin cell and conducting three constant-current charge/discharge cycles at 0.1 C (1 C = 295 mA g^{-1}) within a voltage range of 0.01–2.0 V. Since DMC may have affected the SEI film on the anode surface, DMC cleaning was not performed. DSC tests were conducted at different SOCs, after cycling, and after overdischarge (excessive sodium intercalation into the anode). Meanwhile, DSC tests were also conducted on samples that had been cleaned with DMC for comparison.

To study the influence of composition on the thermal stability of the electrolyte, DSC tests were carried out on electrolytes with different compositions [solvents included propylene carbonate (PC), ethyl methyl carbonate (EMC), and diethyl carbonate (DEC); sodium

salts included sodium hexafluorophosphate (NaFP$_6$) and sodium bis(fluorosulfonyl)imide (NaFSI); and sodium salt concentrations included 0.8 M and 1.0 M]. The test temperature range was 30–380 °C, with a heating rate of 10 °C min^{-1}, and the test environment was under a nitrogen atmosphere.

2.3. Battery Safety Tests

Adiabatic thermal runaway tests were conducted on the NFPP- and NFM-based SIBs using an adiabatic accelerated calorimeter (ARC). The testing procedure was as follows. First, three constant-current charge/discharge cycles were performed on the batteries at 0.1 C (1 C = 3 A) using a Neware 5 V/50 A battery test system (BTS-5 V/50 A, China). The voltage ranges were set at 1.5–3.65 V for the NFPP batteries and 1.5–3.9 V for the NFM batteries. Subsequently, the batteries were charged to 100% SOC. The system then initiated a Heat–Wait–Seek (H–W–S) mode to warm the batteries and monitor their surface temperature rise rate. If the temperature rise rate was less than 0.02 °C min^{-1}, the system heated the batteries by 5 °C and repeated the H–W–S cycle. This process continued until the temperature rise rate reached ≥ 0.02 °C min^{-1}, at which point the instrument ceased active heating and switched to adiabatic mode, tracking the battery's temperature rise until thermal runaway occurred. The test parameters included a 10 min waiting time, a temperature range from 25 °C to 450 °C, and a heat detection sensitivity of 0.02 °C min^{-1}.

3. Results and Discussion

3.1. Thermal Stability Analysis of Electrode Materials and Electrolyte

The DSC test results for the NFPP cathode are shown in Figure 1. In Figure 1a, the DSC curves of the NFPP cathode at 20% and 60% SOC exhibit similar characteristics, both displaying a distinct exothermic peak near 237 °C, with heat generation values of 129.6 J g^{-1} and 118.2 J g^{-1}, respectively. In contrast, the DSC curve of the 100% SOC sample shows significant differences. It features a weak exothermic peak near 259 °C and a strong exothermic peak at 436.6 °C, with a total heat generation of 202.2 J g^{-1}. This indicates that, as the degree of desodiation increases, the oxidation state of Fe gradually rises, leading to an overall upward trend in heat generation [26]. The differences in the DSC curves across SOC levels are likely due to structural phase changes in NFPP caused by variations in sodium content, which alter the thermal stability of the cathode [27]. Figure 1b compares the DSC curves of the NFPP cathode with 100% SOC in the pristine state and aged state. After 50 cycles at a 1 C charge/discharge current, the first weak exothermic peak remains nearly unchanged, while the second main exothermic peak shifts to a temperature approximately 4 °C higher than that of the pristine state. Additionally, the heat generation decreases by about 34%, demonstrating that the thermal stability of NFPP does not degrade with charge–discharge cycling. However, overcharging significantly exacerbates the exothermic reactions of NFPP. As shown in Figure 1a, when overcharged to 120% SOC, the first weak exothermic peak shifts approximately 5 °C lower, and the second strong exothermic peak shifts about 12 °C lower compared to the 100% SOC sample. The heat generation increases by 69.0 J g^{-1}, indicating that excessive desodiation adversely impacts the thermal stability of NFPP. Figure 1c presents the DSC results at different heating rates. As the heating rate increases, the exothermic peaks progressively shift toward higher temperatures. Using data from the main exothermic peaks, Figure 1d is fitted, and the activation energy of the NFPP cathode is calculated to be 98.4 kJ mol^{-1} via the Kissinger equation.
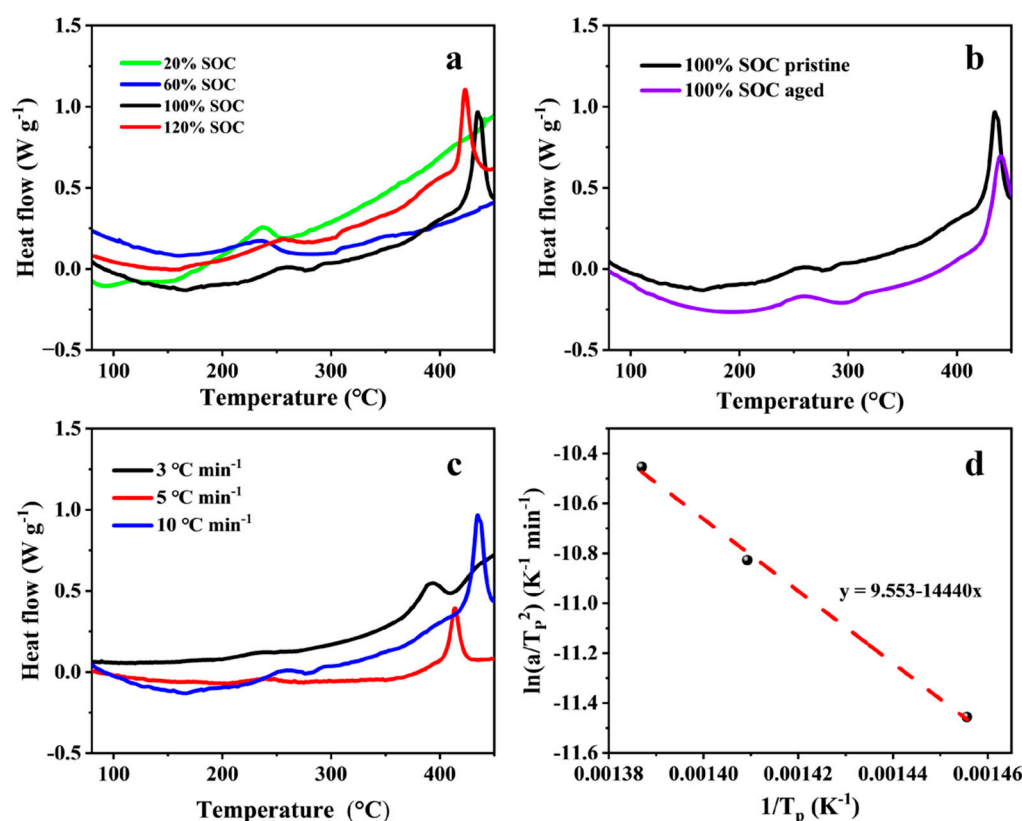
Figure 1. DSC test results of the NFPP cathode: (**a**) NFPP cathode at different SOCs; (**b**) NFPP cathode at 100% SOC before and after 50 cycles at 1C; (**c**) NFPP cathode at 100% SOC under different heating rates; and (**d**) fitting plot of the data from (**c**).

For comparison, the DSC results of the NFM cathode are shown in Figure 2. Similar to NFPP, the DSC curves of NFM at different SOC levels also exhibit significant variations (Figure 2a). The samples at 20% SOC and 60% SOC show weak exothermic peaks at 328 °C and 349 °C, with heat generation values of 60.0 J g^{-1} and 120.6 J g^{-1}, respectively. When the SOC increases to 100%, the peak temperature of the exothermic peak decreases to 323 °C and the heat generation rises markedly to 214.2 J g^{-1}. Additionally, the NFM cathode at 100% SOC displays another exothermic peak at 148 °C, with a corresponding heat generation value as high as 396.6 J g^{-1}. This demonstrates that, as the degree of desodiation increases, the exothermic reactions of NFM intensify significantly. Compared with the thermal stability of NFPP at 100% SOC, NFM is notably lower than that of the NFPP cathode. By referencing the decomposition reactions of lithium-based ternary cathodes, it is inferred that the high-temperature decomposition of NFM likely follows the reaction shown below [22], accompanied by oxygen release. Among the three elements (Ni, Fe, and Mn), Ni is prone to valence changes, suggesting that the reduction of Ni from +4 to +2 may dominate the decomposition process [28].

$$Na_x(NiFeMn)_{1/3}O_2 \rightarrow Na_x(NiFeMn)_{1/3}O_{2-y} + y/2O_2 \qquad (2)$$
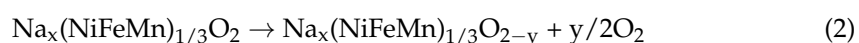
Figure 2b compares the DSC curves of the NFM cathode at 100% SOC in the pristine and aged states. After 50 cycles, the first exothermic peak shifts to a higher temperature, with the peak temperature increasing by approximately 20 °C compared to the pristine sample. The onset and peak temperatures of the second exothermic peak remain nearly unchanged, and the overall heat generation does not increase, indicating that cycling does not adversely affect the thermal stability of the NFM cathode. As shown in Figure 2a, when the NFM cathode is overcharged to 120% SOC, heat generation begins at 233 °C and reaches

a peak at 306 °C, with a heat generation value of 321.6 J g^{-1}. Compared to the 100% SOC sample, this exothermic peak occurs at a lower temperature with increased heat generation, confirming that overcharging degrades the thermal stability of the NFM cathode. Figure 2c characterizes the thermal stability of the NFM cathode at different heating rates. Based on the main exothermic peak data, Figure 2d is fitted, and the activation energy of the NFM cathode is calculated to be 72.1 kJ mol^{-1} using the Kissinger equation.
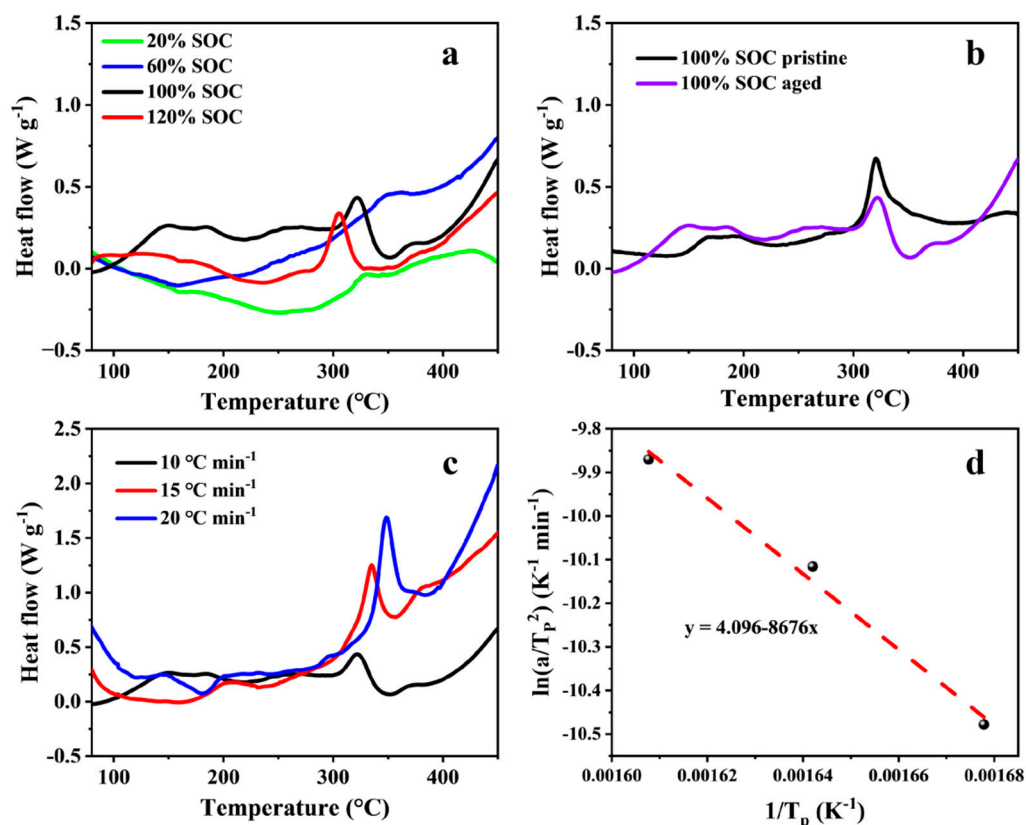
Figure 2. DSC test results of NFM cathode: (**a**) NFM cathode at different SOCs; (**b**) NFM cathode at 100% SOC before and after 50 cycles at 1C; (**c**) NFM cathode at 100% SOC under different heating rates; and (**d**) fitting plot of the data from (**c**).

The DSC curves of the hard carbon anode are presented in Figure 3. DSC measurements initiated at 50 °C reveal a prominent exothermic peak at 57 °C for the 60% SOC HC anode, absent in the 20% and 100% SOC samples. This phenomenon is attributed to reactive sodium intermediates formed during partial intercalation and SEI maturation at an intermediate SOC. At 20% SOC, insufficient sodium intercalation precludes detectable reactivity, while at 100% SOC, ionic-state sodium storage and a stabilized SEI mitigate exothermic processes. As shown in Figure 3a, the HC anode exhibits two distinct exothermic peaks at different SOC levels. The first exothermic peak starts at 116–120 °C, which is speculated to correspond to the thermal decomposition of the SEI film on the anode surface. The formation and growth mechanism of SEI films in sodium-ion batteries remain controversial, but their composition is generally considered as similar to that in lithium-ion batteries, consisting of inorganic components (such as Na_2O, NaF, and Na_2CO_3) and organic components (such as $RONa$, $ROCO_2Na$, and $RCOONa$) [29]. Due to its high thermal sensitivity, the organic component ratio in the SEI film of sodium-ion batteries is higher [30]. Assuming that the main component of the SEI film is $(CH_2OCO_2Na)_2$, the possible decomposition reaction equation is as follows:

$$(CH_2OCO_2Na)_2 \rightarrow Na_2CO_3 + CO_2 + C_2H_4 + 1/2O_2 \tag{3}$$
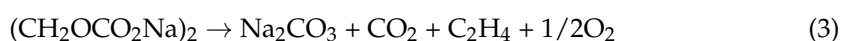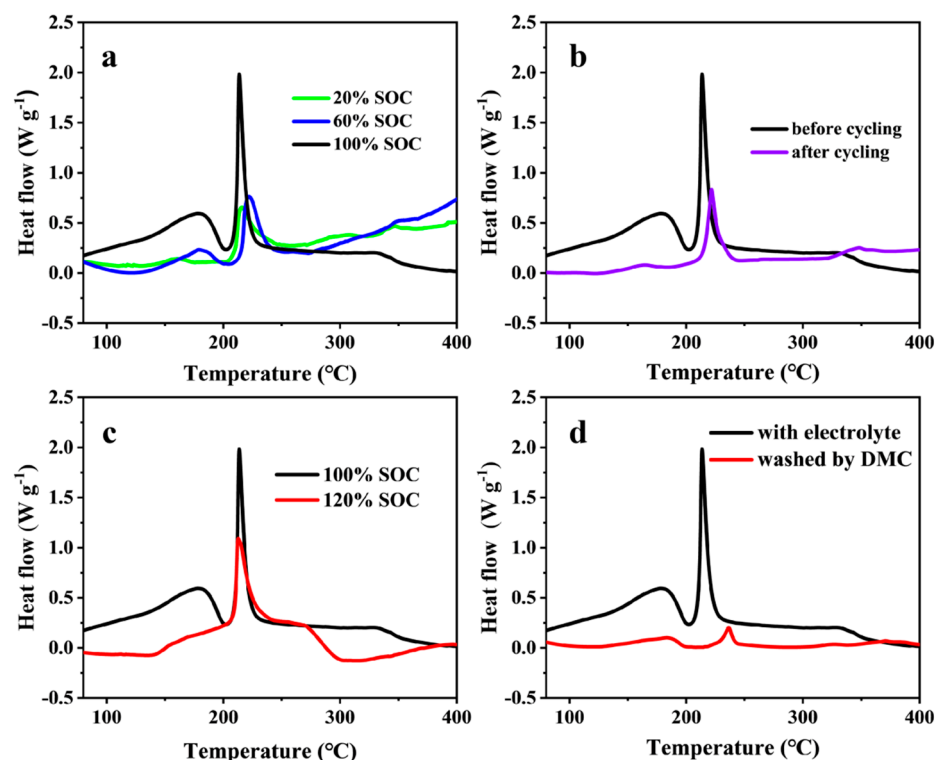
Figure 3. DSC test results of hard carbon anode: (**a**) HC anode at different SOCs; (**b**) HC anode at 100% SOC before and after 50 cycles at 1C; (**c**) HC anode at 100% and 120% SOCs; and (**d**) HC anode at 100% SOC before and after DMC washing.

The second exothermic peak appears after 200 °C, with a peak temperature of 211–216 °C. The sample used here is not washed with DMC, meaning that the electrode contains absorbed electrolyte. After SEI decomposition, the active material of the anode loses its protective layer, and the intercalated sodium may react with the electrolyte, generating a sparse SEI film and leading to the second exothermic peak. When the solvent in the electrolyte is PC, the possible reaction equation between metallic sodium and the electrolyte is as follows:

$$2Na + C_4H_6O_3 \rightarrow Na_2CO_3 + C_3H_6 \tag{4}$$
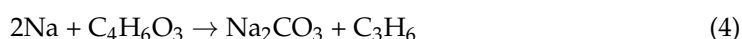
As SOC increases, the total heat release of both exothermic peaks shows an increasing trend, with total heat release values of 346.8, 582.6, and 844.2 J g^{-1} at 20%, 60%, and 100% SOC, respectively. The DSC test results of the HC anode with 100% SOC before and after 50 cycles (Figure 3b) indicate that cycling does not negatively impact the thermal stability of the anode, and the total heat release slightly decreases. Unlike the cathode, Figure 3c demonstrates that the exothermic reaction temperature of the over-sodiated hard carbon anode does not decrease, though the DSC curve shape changes and the total heat release increases by approximately 70% compared to the 100% SOC condition. Figure 3d compares the impact of DMC washing on the DSC test results of the anode. The significant reduction in the first exothermic peak suggests that DMC washing has a notable destructive effect on the SEI film, which also confirms the existence of the SEI film on the anode surface. Furthermore, after DMC washing and drying, most of the electrolyte in the anode is removed, leading to a significant reduction in the heat release corresponding to the second exothermic peak. This observation is consistent with studies on lithium-ion batteries with lithium-intercalated graphite anodes [31].

Figure 4 presents the DSC test curves of sodium-ion battery electrolytes. We compare the thermal stability of electrolytes composed of several commonly used sodium salts and solvents, as well as the effects of different sodium salt concentrations. As shown in Figure 4a, regarding the type of sodium salt, when the solvent and sodium salt concentration are the same, the electrolyte using $NaPF_6$ exhibits a higher thermal stability than that using NaFSI [32]. Regardless of whether the sodium salt concentration is 0.8 M or 1.0 M, the NaFSI-based electrolyte shows a noticeable exothermic peak before 200 °C, whereas the $NaPF_6$-based electrolyte exhibits a strong exothermic peak around 320 °C. In terms of the solvent type, when the sodium salt concentration is fixed at 1.0 M $NaPF_6$, the onset temperature of exothermic reactions is slightly lower for mixed solvents such as PC/EMC, PC/EMC/DEC, and PC/DMC/DEC compared to the pure PC solvent (Figure 4b). However, the total heat release of mixed solvents is lower than that of the pure PC solvent. Finally, regarding the sodium salt concentration, increasing the concentration of $NaPF_6$ or NaFSI slightly lowers the exothermic temperature of the electrolyte. The above findings on the effects of solvent and sodium salt concentration are consistent with research reports on lithium-ion battery electrolytes [33]. It is important to note that, in this study, the baseline electrolyte for pouch-type sodium-ion batteries is 0.8 M NaFSI/PC, with multiple functional additives included. These additives may influence the overall thermal stability of the electrolyte.
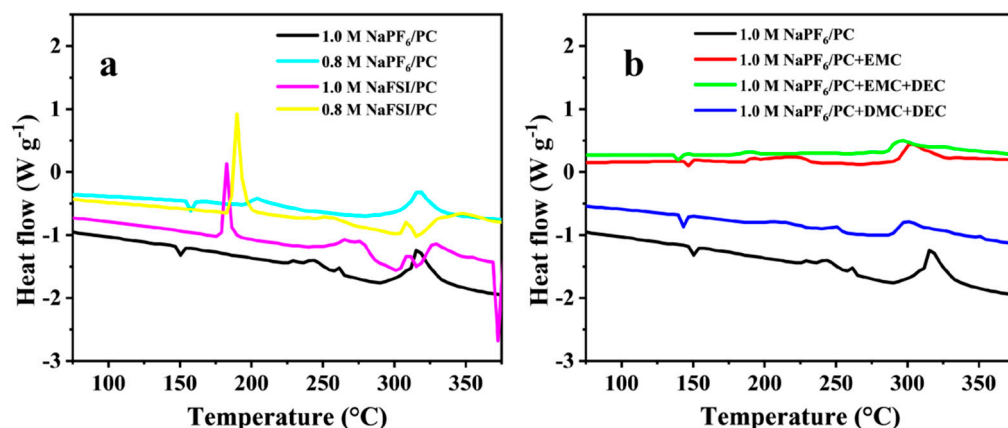

Figure 4. The DSC test results for different electrolytes in sodium-ion batteries: (**a**) different sodium salts with different concentrations in PC solvent and (**b**) 1.0 M $NaPF_6$ in different solvents.

3.2. Analysis of Battery Thermal Runaway Behavior

Figure 5 presents the accelerating rate calorimetry (ARC) test results of the pouch-type battery based on the NFPP cathode and HC anode. Based on the trends in temperature, voltage, and heating rate, the thermal runaway process of this battery is divided into four stages, as shown in Figure 5. Stage I lasts from the start of the experiment to the point where a significant voltage drop occurs. During this stage, exothermic side reactions generate heat that accumulates inside the battery, causing the separator to shrink and deform, leading to localized internal short circuits. As a result, the voltage drops sharply from 3.3 V to 1.3 V. It is worth noting that the initial voltage is relatively low, possibly due to self-discharge from prolonged storage before testing [21]. The heating rate has not yet reached the set threshold in this stage, and the temperature curve exhibits a step-like pattern. Stage II lasts from the onset of the voltage drop until the voltage reaches 0 V, corresponding to a temperature range from 140.7 °C to 187.5 °C. Shortly after this stage begins, the detected heating rate reaches 0.02 °C min^{-1}, marking entry into the adiabatic tracking phase. According to Figure 5b, the onset temperature of self-heating (T_1) is 151.0 °C. The first two stages reveal that a significant voltage drop occurs before the appearance of T_1. This suggests that, in pouch cells, gas generation during heating causes swelling, leading to a discrepancy

between the measured surface temperature and the internal temperature of the battery. Consequently, self-heating reactions may have already started before entering the adiabatic tracking phase, causing the measured T_1 value to be relatively high [34]. Stage III lasts from the voltage drop to 0 V until the battery reaches its peak temperature ($T_3 = 303.5\ ^\circ$C). In this stage, exothermic side reactions intensify, leading to a rapid temperature increase. Notably, the maximum heating rate (T_{cmax}) observed in this experiment is 0.10 $^\circ$C s^{-1} at a battery temperature of 235.5 $^\circ$C. Conventionally, the thermal runaway onset temperature (T_2) is defined as the temperature at which the heating rate reaches 1 $^\circ$C s^{-1}. However, in this experiment, T_2 does not appear, indicating that the thermal runaway process of NFPP-based batteries is relatively mild. Stage IV lasts from the peak temperature to the end of the experiment. During this phase, the battery temperature gradually decreases.
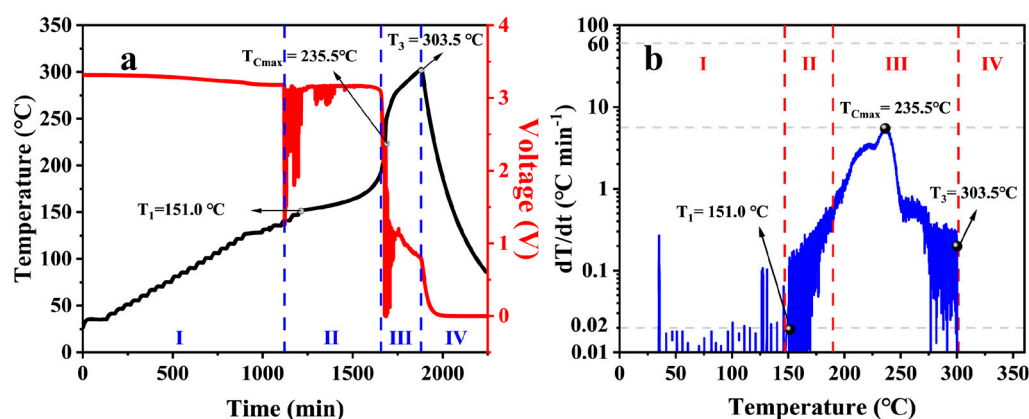

Figure 5. ARC test results of NFPP-based battery: (**a**) temperature (black) and voltage (red) variation over time and (**b**) relationship between heating rate and temperature.

To analyze the exothermic reactions corresponding to the thermal runaway process from the perspective of the intrinsic thermal stability of key materials, Figure 6 categorizes the DSC curves of the NFPP cathode, HC anode, and electrolyte (0.8 M NaFSI/PC) according to the temperature ranges of each thermal runaway stage. Stage I consists of heat accumulation primarily resulting from the first exothermic peak of the HC anode (SEI decomposition). In Stage II, SEI decomposition continues, and the electrolyte begins to decompose, increasing the heating rate and causing separator melting, which leads to a sudden voltage drop. In Stage III, exothermic reactions between the HC anode and the electrolyte intensify, and the electrolyte decomposition continues. Meanwhile, the NFPP cathode exhibits its first exothermic peak. Various materials contribute to heat accumulation, driving the battery to its highest temperature. In Stage IV, the battery temperature starts to decline. Notably, the test does not reach the main exothermic peak of the NFPP cathode, suggesting that it has a good thermal stability and a relatively small contribution to thermal runaway.

As shown in Figure 7a, the adiabatic thermal runaway of the NFM-based battery exhibits distinct characteristics compared to the NFPP-based battery, and its process is divided into six stages. Stage I lasts from the start of the experiment to a slight voltage drop (from room temperature to 140.8 $^\circ$C). This voltage drop may be due to the loss of active material. Stage II lasts from this slight voltage drop to a significant voltage drop (147.8 $^\circ$C). Continuous exothermic reactions cause heat accumulation, leading to separator melting and shrinkage, which induces local short circuits and accelerates voltage reduction. Stage III lasts from the significant voltage drop to a sharp drop to 0 V (147.8 $^\circ$C to 221.0 $^\circ$C). The voltage remains around 3.14 V with small fluctuations before dropping to 0 V. At 1438 min, the heating rate reaches 0.02 $^\circ$C min^{-1}, marking the entry into adiabatic tracking. The onset

temperature of self-heating (T_1) is 177.9 °C. Similar to the NFPP-based battery, actual self-heating likely starts before T_1. Stage IV lasts from the sharp voltage drop to 0 V until thermal runaway. The magnified view in Figure 7b shows large voltage fluctuations between 3 V and 0 V, while the temperature increases slowly. As shown in Figure 7c, the thermal runaway onset temperature (T_2) is 233.2 °C when the heating rate reaches 1 °C s^{-1}. Stage V lasts from thermal runaway onset to the peak temperature ($T_3 = 409.8$ °C). The voltage finally drops to 0 V, and the heating rate increases rapidly, peaking at 9.7 °C s^{-1}. Compared to the NFPP-based battery, the NFM-based battery undergoes a more intense thermal runaway reaction, reaching its peak temperature in less than 40 s. Stage VI lasts from the peak temperature to the end of the experiment, with the temperature gradually decreasing.
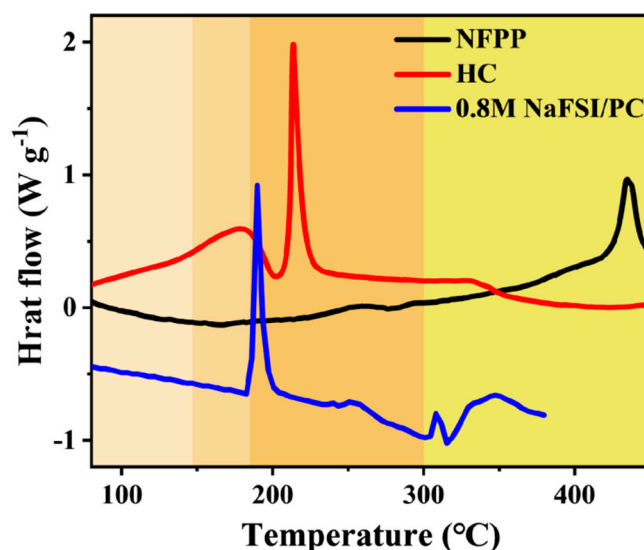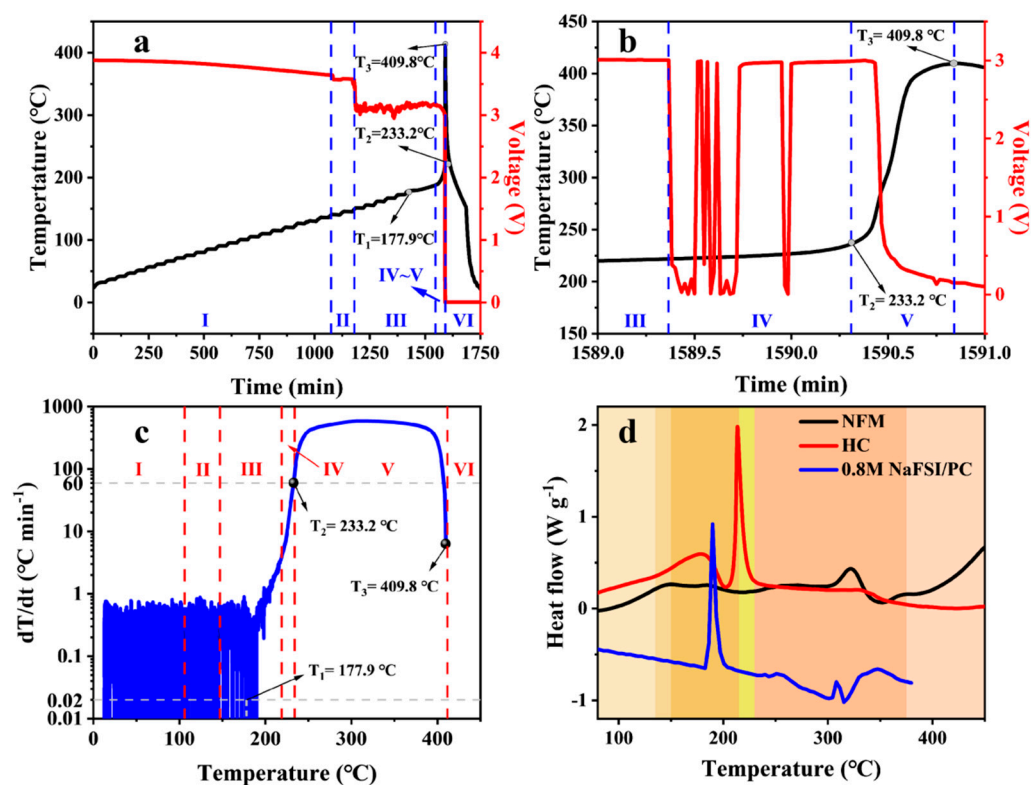

Figure 6. DSC curves of electrode and electrolyte in different stages of NFPP-based battery during thermal runaway process.

Figure 7d displays the DSC curves of the NFM cathode, HC anode, and electrolyte in different stages during the thermal runaway process. In Stage I, decomposition reactions occur in both the NFM cathode and the SEI layer of the HC anode, leading to active material loss and a decrease in battery voltage. In Stage II, the first exothermic peaks of both the cathode and anode continue, causing heat accumulation and accelerating the voltage drop. In Stage III, the first exothermic peak of the NFM cathode generates a significant amount of heat. Meanwhile, the HC anode undergoes an exothermic reaction between metallic sodium and the electrolyte, while the electrolyte also decomposes. The accumulated heat from multiple exothermic reactions melts the separator, reducing the battery voltage to 0 V. In Stage IV, the above reactions continue, and oxygen and flammable gases generated from decomposition accumulate, triggering thermal runaway. In Stage V, the second exothermic peak of the NFM cathode dominates, leading to the highest temperature and fastest heating rate, indicating that the NFM cathode significantly contributes to battery thermal runaway. In Stage VI, the battery temperature decreases. At temperatures above T_3, no further exothermic peaks are observed for any materials.

Table 2 summarizes the ARC test results for the two types of SIBs. Before entering the adiabatic tracking mode, both the NFPP- and NFM-based batteries showed voltage drops to varying degrees, and the temperatures at which this phenomenon was initially detected were quite close. This indicates that the actual self-heat generation and accumulation in these two types of batteries occurred before the temperature corresponding to the earliest voltage drop, but the specific values are uncertain. Therefore, it is difficult to judge the relative magnitudes of the self-heat generation starting temperatures of the two types of

batteries based on T_1. The thermal runaway starting temperature T_2 of the NFM-based battery was 233.2 °C, while the temperature rise rate of the NFPP-based battery did not reach the thermal runaway judgment standard (1 °C s^{-1}) and its temperature rise was relatively slow throughout the thermal runaway process. The maximum temperature rise rate was only 0.15 °C s^{-1}, which is much lower than that of the NFM-based battery, indicating that the heat-generating reaction of the NFPP-based battery was relatively mild. In addition, the maximum temperature T_3 during the thermal runaway of the NFM-based battery was also higher than that of the NFPP-based battery, indicating that its thermal runaway was more harmful.

Figure 7. ARC test results for NFM-based battery: (**a**) temperature (black) and voltage (red) variation over time, (**b**) magnified view of (**a**), (**c**) relationship between heating rate and temperature; and (**d**) DSC curves of electrode and electrolyte in different stages of NFM-based battery during thermal runaway process.

Table 2. Summary of ARC test results for NFPP- and NFM-based batteries.

Battery Type	Earliest Phenomenon (Temperature °C)	T_1/°C	T_2/°C	T_3/°C	Max Heating Rate (°C·s^{-1})
NFPP/HC	Voltage drop (140.7)	151.0	/	303.5	0.15
NFM/HC	Voltage drop (140.8)	177.9	233.2	409.8	9.70

4. Conclusions

This study investigates the thermal stability of key materials and the thermal runaway characteristics of NFPP- and NFM-based sodium-ion batteries. Key findings reveal that SOC strongly influences cathode stability—heat generation rises with sodium extraction, while constant-current cycling minimally impacts stability. However, overcharging drastically reduces thermal stability in both cathodes. DSC analysis shows that NFPP and NFM have distinct activation energies (98.4 kJ mol^{-1} vs. 72.1 kJ mol^{-1}), indicating NFPP's superior resistance to thermal degradation. The HC anode contributes to thermal runaway through

SEI decomposition and exothermic sodium–electrolyte reactions. Electrolyte composition also plays a critical role—NaPF$_6$-based electrolytes outperform NaFSI variants in terms of thermal stability, though higher salt concentrations lower exothermic onset temperatures. Solvent mixtures (e.g., EMC, DEC, and DMC) exhibit a reduced stability compared to pure PC. Under adiabatic conditions, the NFPP/HC system undergoes thermal runaway in four stages, with onset T$_1$ at 151.0 °C, a peak heating rate (0.15 °C s^{-1}) at 235.5 °C, and a maximum temperature T$_3$ at 303.5 °C. NFPP demonstrates a robust thermal stability, contributing minimally to thermal runaway progression. In contrast, the NFM/HC system exhibits a more severe six-stage thermal runaway process, as follows: T$_1$ = 177.9 °C, T$_2$ = 233.2 °C, and T$_3$ = 409.8 °C, with the NFM cathode driving significant heat release. Comparative analysis highlights NFPP's milder thermal runaway profile, characterized by lower heating rates and overall hazard potential than NFM. These differences underscore the critical role of cathode chemistry in thermal runaway severity, emphasizing NFPP's suitability for safer battery designs. The findings provide actionable insights for optimizing material selection, electrolyte formulations, and safety protocols in SIB development.

References

1. Larcher, D.; Tarascon, J. Towards greener and more sustainable batteries for electrical energy storage. *Nat. Chem.* **2015**, *7*, 19–29. [CrossRef] [PubMed]
2. Kammen, D.; Sunter, D.A. City-integrated renewable energy for urban sustainability. *Science* **2016**, *352*, 922–928. [CrossRef]
3. Huang, Z.H.; Li, H.; Mei, W.X.; Zhao, C.; Sun, J.; Wang, Q. Thermal runaway behavior of lithium iron phosphate battery during penetration. *Fire Technol.* **2020**, *56*, 2405–2426. [CrossRef]
4. Wu, X.; Meledina, M.; Barthel, J.; Liu, Z.; Tempel, H.; Kungl, H.; Mayer, J.; Eichel, R.A. Investigation of the Li-Co antisite exchange in Fe-substituted LiCoPO$_4$ cathode for high-voltage lithium ion batteries. *Energy Storage Mater.* **2019**, *22*, 138–146. [CrossRef]
5. Wu, X.; Meledina, M.; Tempel, H.; Kungl, H.; Mayer, J.; Eichel, R.A. Morphology-controllable synthesis of LiCoPO$_4$ and its influence on electrochemical performance for high-voltage lithium ion batteries. *J. Power Sources* **2020**, *450*, 227726. [CrossRef]
6. Pu, X.; Wang, H.; Yuan, T.; Cao, S.; Liu, S.; Xu, L.; Yang, H.; Ai, X.; Chen, Z.; Cao, Y. Na$_4$Fe$_3$(PO$_4$)$_2$P$_2$O$_7$/C nanospheres as low-cost, high-performance cathode material for sodium-ion batteries. *Energy Storage Mater.* **2019**, *22*, 330–336. [CrossRef]
7. Chen, S.; Wu, C.; Shen, L.; Zhu, C.; Huang, Y.; Xi, K.; Maier, J.; Yu, Y. Challenges and Perspectives for NASICON-Type Electrode Materials for Advanced Sodium-Ion Batteries. *Adv. Mater.* **2017**, *29*, 1700431. [CrossRef] [PubMed]
8. Wang, K.; Wang, C.; Yang, H.; Wang, X.; Cao, F.; Wu, Q.; Peng, H. Vertical graphene nanosheetsmodified Al current collectors for high-performance sodium-ion batteries. *Nano Research* **2020**, *13*, 1948–1954. [CrossRef]
9. Song, I.T.; Kang, J.; Koh, J.; Choi, H.; Yang, H.; Park, E.; Lee, J.; Cho, W.; Lee, Y.M.; Lee, S.; et al. Thermal runaway prevention through scalable fabrication of safety reinforced layer in practical Li-ion batteries. *Nat. Commun.* **2024**, *15*, 8294. [CrossRef]
10. Ye, Z.; Fu, X. Experimental and simulation investigation on suppressing thermal runaway in battery pack. *Sci. Rep.* **2024**, *14*, 12723. [CrossRef]
11. Edge, J.S.; O'Kane, S.; Prosser, R.; Kirkaldy, N.D.; Patel, A.N.; Hales, A.; Ghosh, A.; Ai, W.; Chen, J.; Yang, J.; et al. Lithium ion battery degradation: What you need to know. *Phys. Chem. Chem. Phys.* **2021**, *23*, 8200–8221. [CrossRef]
12. Zhu, Y.; Wang, Z.; Bian, H.; Wang, J.; Bai, W.; Gao, T.; Bai, J.; Zhou, Y. Critical conditions for the thermal runaway propagation of lithium-ion batteries in air and argon environments. *J. Therm. Anal. Calorim.* **2022**, *147*, 13699–13710. [CrossRef]

13. Kong, J.; Liu, J.; Zhu, J.; Zhang, X.; Tsui, K.L.; Peng, Z.; Wang, D. Review on lithium-ion battery PHM from the perspective of key PHM Steps. *Chin. J. Mech. Eng.* **2024**, *37*, 71. [CrossRef]

14. Liu, J.; Huang, Z.; Sun, J.; Wang, Q. Heat generation and thermal runaway of lithium-ion battery induced by slight overcharging cycling. *J. Power Sources* **2022**, *526*, 231136. [CrossRef]

15. Tao, C.; Chen, Z.; Ye, Q.; Li, G.; Zhang, Y.; Liu, Y. The study of thermal runaway characteristics of multiple lithium batteries under different immersion times. *J. Therm. Anal. Calorim.* **2022**, *147*, 11457–11466. [CrossRef]

16. Kong, L.; Li, Y.; Feng, W. Strategies to solve lithium battery thermal runaway: From mechanism to modification. *Electrochem. Energy Rev.* **2021**, *4*, 633–679. [CrossRef]

17. Ren, D.; Liu, X.; Feng, X.; Lu, L.; Ouyang, M.; Li, J.; He, X. Model-based thermal runaway prediction of lithiumion batteries from kinetics analysis of cell components. *Appl. Energy* **2018**, *228*, 633–644. [CrossRef]

18. Robinson, J.B.; Finegan, D.P.; Heenan, T.M.; Smith, K.; Kendrick, E.; Brett, D.J.; Shearing, P.R. Microstructural analysis of the effects of thermal runaway on Li-ion and Na-ion battery electrodes. *J. Electrochem. Energy Convers. Storage* **2018**, *15*, 011010. [CrossRef]

19. Huang, Y.; Zhang, Q.; Sun, X.G.; Liu, K.; Sun, W.; Zhi, M.; Guo, Y.; Zheng, S.; Dai, S. Multiple functional bonds integrated interphases for long cycle sodium-ion batteries. *Angew. Chem. Int. Ed.* **2024**, *63*, e202406277. [CrossRef]

20. Gan, Y.; Ping, P.; Wang, J.; Song, Y.; Gao, W. Comparative analysis of thermal stability and electrochemical performance of $NaNi_{1/3}Fe_{1/3}Mn_{1/3}O_2$ cathode in different electrolytes for sodium ion batteries. *J. Power Sources* **2024**, *594*, 2340. [CrossRef]

21. Yue, Y.; Jia, Z.; Li, Y.; Wen, Y.; Lei, Q.; Duan, Q.; Sun, J.; Wang, Q. Thermal runaway hazards comparison between sodium-ion and lithium-ion batteries using accelerating rate calorimetry. *Process Saf. Environ. Prot.* **2024**, *189*, 61–70. [CrossRef]

22. Gui, Q.; Xu, B.; Yu, K.; Wang, X.; Li, J.; Xie, Y.; Yu, R.; Zhou, X.; Mao, L. Comparison of $NaNi_{1/3}Fe_{1/3}Mn_{1/3}O_2$ and $Na_4Fe_3(PO_4)_2(P_2O_7)$ cathode sodium-ion battery behavior under overcharging induced thermal runaway. *Chem. Eng. J.* **2024**, *497*, 154732. [CrossRef]

23. Zhao, X.X.; Fu, W.; Zhang, H.X.; Guo, J.Z.; Gu, Z.Y.; Wang, X.T.; Yang, J.L.; Lü, H.Y.; Wu, X.L.; Ang, E.H. Pearl-structure-enhanced NASICON cathode toward ultrastable sodium-ion batteries. *Adv. Sci.* **2023**, *10*, 2301308. [CrossRef]

24. Gu, Z.Y.; Wang, X.T.; Heng, Y.L.; Zhang, K.Y.; Liang, H.J.; Yang, J.L.; Ang, E.H.; Wang, P.F.; You, Y.; Du, F.; et al. Prospects and perspectives on advanced materials for sodium-ion batteries. *Sci. Bull.* **2023**, *68*, 2302–2306. [CrossRef]

25. Su, M.Y.; Zhang, K.Y.; Ang, E.H.; Zhang, X.L.; Liu, Y.N.; Yang, J.L.; Gu, Z.Y.; Butt, F.A.; Wu, X.L. Structural regulation of coal-derived hard carbon anode for sodium-ion batteries via pre-oxidation. *Rare Met.* **2024**, *43*, 2585–2596. [CrossRef]

26. Li, Z.; Zhang, Y.; Wang, Y. High-power and low-cost sodium-ion batteries with a wide operation temperature from $-70\,^{\circ}C$ to $130\,^{\circ}C$. *SmartMat* **2023**, *4*, e1191. [CrossRef]

27. Teng, A.; Zhang, Y.; Jiang, L.; Dang, H.; Wang, C.; Fang, Z.; Liu, Y.; Wang, X.; Li, H.; Mei, W.; et al. Revealing the thermal stability of sodium-ion battery from material to cell level using combined thermal-gas analysis. *J. Energy Chem.* **2025**, *103*, 838–849. [CrossRef]

28. Chen, M.; Zhao, C.; Li, Y.; Wang, H.; Wang, K.; Yang, S.; Gao, Y.; Zhang, W.; Chen, C.; Zhang, T.; et al. Breaking boundaries in O3-type $NaNi_{1/3}Fe_{1/3}Mn_{1/3}O_2$ cathode materials for sodium-ion batteries: An industrially scalable reheating strategy for superior electrochemical performance. *J. Energy Chem.* **2025**, *102*, 107–119. [CrossRef]

29. Bao, C.; Wang, B.; Liu, P.; Wu, H.; Zhou, Y.; Wang, D.; Liu, H.; Dou, S. Solid electrolyte interphases on sodium metal anodes. *Adv. Funct. Mater.* **2020**, *30*, 2004891. [CrossRef]

30. Yang, C.; Xin, S.; Mai, L.; You, Y. Materials design for high-safety sodium-ion battery. *Adv. Energy Mater.* **2021**, *11*, 2000974. [CrossRef]

31. Waldmann, T.; Hogg, B.-I.; Wohlfahrt-Mehrens, M. Li plating as unwanted side reaction in commercial Li-ion cells—A review. *J. Power Sources* **2018**, *384*, 107–124. [CrossRef]

32. Eshetu, G.G.; Grugeon, S.; Kim, H.; Jeong, S.; Wu, L.; Gachot, G.; Laruelle, S.; Armand, M.; Passerini, S. Comprehensive Insights into the Reactivity of Electrolytes Based on Sodium Ions. *ChemSusChem* **2016**, *9*, 462–471. [CrossRef] [PubMed]

33. Shen, Y.; Xu, J.; Li, Y.; Zhao, S.; Che, H.; Maher, J.; Wang, X.; Zhang, Y.; Wu, J.; Li, J.; et al. Adjusting anion-solvent dipole interactions in ether-based electrolytes for wide temperature range applications of sodium-ion batteries. *J. Mater. Chem. A* **2024**, *12*, 33559–33571. [CrossRef]

34. Faseena, A.M.; Sreekumar, A. Advances, perspectives and challenges in phase change material based battery thermal management: A comprehensive review. *J. Energy Storage* **2025**, *113*, 115644. [CrossRef]